Exploring the performance of thin-film superconducting multilayers as Kinetic Inductance Detectors for low-frequency detection

Songyuan Zhao,[1,*] D. J. Goldie,[1] S. Withington,[1] and C. N. Thomas[1]

[1] *Cavendish Laboratory, JJ Thomson Avenue, Cambridge CB3 OHE, United Kingdom.*

(Dated: March 7, 2024)

We have solved numerically the diffusive Usadel equations that describe the spatially-varying superconducting proximity effect in Ti − Al thin-film bi- and trilayers with thickness values that are suitable for Kinetic Inductance Detectors (KIDs) to operate as photon detectors with detection thresholds in the frequency range of 50−90 GHz. Using Nam's extension of the Mattis-Bardeen calculation of the superconductor complex conductivity, we show how to calculate the surface impedance for the spatially varying case, and hence the surface impedance quality factor. In addition, we calculate energy-and spatially-averaged quasiparticle lifetimes at temperatures well-below the transition temperature and compare to calculation in Al. Our results for the pair-breaking threshold demonstrate differences between bilayers and trilayers with the same total film thicknesses. We also predict high quality factors and long multilayer-averaged quasiparticle recombination times compared to thin-film Al. Our calculations give a route for designing KIDs to operate in this scientifically-important frequency regime.

PACS numbers: 07.57.Kp, 74.45.+c, 74.78.Fk, 85.25.-j
Keywords: Kinetic Inductance Detectors, Superconducting proximity effect, Surface impedance, Recombination time, Usadel equations

arXiv:1708.03234v2 [cond-mat.supr-con] 19 Oct 2017

I. INTRODUCTION

Kinetic Inductance Detectors (KIDs) are thin-film superconducting devices, typically $\sim$ 100 nm-thick, that can be configured as ultra-sensitive detectors for astronomical observations across the electromagnetic spectrum.[1] They are readily fabricated by conventional ultra-high vacuum deposition techniques and can be patterned using optical lithography. KID operating temperatures are low ($T \sim 1$ K or below) giving excellent performance in terms of energy resolution when used as microcalorimeters, or noise equivalent power when used as bolometers. Achieving ultimate performance and low noise requires that the operating temperature satisfies $T/T_c \lesssim 0.15$, where T_c is the superconducting transition temperature. Low operating temperatures ensure sufficiently long quasiparticle recombination times τ_r such that the quasiparticle generation-recombination noise is minimized and signal-to-noise is maximized.[2–6] In practice the minimum operating temperature T_b is determined by available cryogenic technology, so that $T_b \simeq 60$ mK using an adiabatic demagnetization refrigerator (ADR), or a dilution refrigerator, has become a practical lower-bound for experiments sited in remote high-altitude terrestrial observatories or on satellites. The photon detection threshold of a KID is determined by the requirement that the photon has sufficient energy to break a Cooper pair $h\nu \geq 2\Delta_g$, where h is Planck's constant, ν is the frequency of the detected radiation, and Δ_g is the superconducting energy gap. Each broken pair creates two excess quasiparticles, and the timescale for the recombination of the excess back into pairs, whilst emitting phonons, is determined by τ_r. The effect of pair-breaking can be detected by configuring the superconductor into a thin-film L − C resonator that is readout by a low frequency microwave probe (typically $1-10$ GHz) close to the circuit resonant frequency f_0. A change in the number of pairs, changes the superconductor complex conductivity σ, surface impedance Z_s, quality factor Q, and f_0, and can be observed in the through-transmission of the probe circuit. The advantage of the scheme is that as few as two coaxial lines are required to connect from the room temperature to T_b to readout an array. The readout readily lends itself to frequency domain multiplexing. High detector Q values are required to achieve high responsivity, high sensitivity, and high multiplexing factors.[1,2]

There exists a particular challenge in the design of KIDs as low frequency detectors for Cosmic Microwave Background observations at $\sim 70-120$ GHz from the ground, or on a satellite,[7,8] for measurement of low redshift CO lines at around $100-110$ GHz,[9,10] or for measurements of O_2 rotation lines at $50-60$ GHz for atmospheric profiling.[11–13] At the detection threshold frequency $\nu_g = 2\Delta_g/h$, the details of the photon-Cooper pair interaction matrix (the so-called case II interaction) mean that the interaction probability is vanishingly-small at low temperatures and increases towards the normal-state value only slowly as a function of ν.[14] Using the Bardeen-Cooper-Schrieffer (BCS) result $\Delta_g = 1.76\, k_B T_c$ where k_B is Boltzmann's constant, the constraints on T_c determined by bath temperature and pair-breaking threshold can be parameterized as $7\, T_b \lesssim T_c \leq \kappa\nu_g$. κ depends on geometry, such that, for direct absorption, $\kappa \simeq 14$ mK/GHz at threshold, reducing to $\simeq 10$ mK/GHz if a margin of 25% is adopted to achieve a pair-breaking efficiency of order 30% of the normal-state value (see Fig. 6 later). There are few elemental superconductors with the required T_c ($\sim 500-900$ mK) that satisfy these constraints. For example, Al with T_c of 1.2 K has a detection *threshold* of 88 GHz. Current solutions

to this problem have been to use alloy superconductors, such as AlMn,[15] or reactively sputtered materials such as TiN,[16] such that T_c and Δ_g can be adjusted to the application. But these sub-stoichiometric compounds have shown wide variations in their properties even in a single deposition,[17] and the current preferred solution is to use multilayers consisting of pure Ti and stoichiometric TiN.[18,19] For transition edge sensors where it is necessary to tune T_c, the most-common technological solution is a metallic bi- or trilayer where the properties of a superconducting film S are modified by the superconducting proximity effect due to its close electronic contact to a lower-gap superconducting or normal metal S′. Cooper pairs diffuse from S into S′, changing the overall superconducting properties of the composite. Catalano *et al.*[8] have recently explored this approach in the context of Al/Ti KIDs. Their prediction for the energy gap of the bilayer used Cooper's model[20] to calculate the weighted-average electron-phonon coupling constant $\overline{N_0V}$ (N_0 is the single-spin density of electron states at the Fermi energy and V is the interaction potential). The usual BCS self-consistency expression was then used to solve for T_c[14] and hence Δ_g. We will refer to this approach as the "weighted-average model".

A full analysis of a multilayer resonator for use as a KID requires a proper account of the spatial variation of its superconducting properties as a function of position through the film, x. The best approach to this problem is to solve the one-dimensional diffusive Usadel equations with appropriate boundary conditions.[21–25] This is the approach we use here. For simplicity we concentrate on $\mathrm{Ti}-\mathrm{Al}$ bilayers and $\mathrm{Al}-\mathrm{Ti}-\mathrm{Al}$ trilayers although the method would apply for any material combinations that can be described by BCS superconductivity. We compare the results of these proximity structures with that of Al, since the properties of Al are well characterised, both as a BCS superconductor, and as a mature KID system (e.g. NIKA).[26,27]

In Sec.II we outline the theoretical basis of the model. This allows us to calculate the spatial variation of the superconducting order parameter $\Delta(x)$, the quasiparticle and pair densities of states, and the superconducting energy gap Δ_g. We show how to calculate the complex conductivity $\sigma(x)$ and the surface impedance Z_s taking account of spatially varying film properties. We discuss how to take account of the ordering of a multilayer with respect to the incident field. From Z_s we calculate the surface impedance quality factor Q_s. We calculate the position and energy dependent quasiparticle recombination time $\tau_r(x,E)$ (E is the energy) and introduce expressions for energy- and multilayer-averaging of τ_r. Throughout these calculations we take full account of the spatial variation of the material parameters T_c, N_0, normal-state conductivity σ_N, and characteristic quasiparticle recombination time τ_0 for dissimilar materials. Whilst some of these equations have been described previously, here we present a consistent formulation using a common framework. This is essential and means that the model described reduces to more usual expressions in the homogeneous BCS limit.

Section III gives details of the numerical method and material parameters and we discuss the temperature scaling used to ensure that calculations of the properties of multilayers with different ν_g are done in comparable temperature regimes. In Sec. IV we show some of the most important outcomes of the modeling. The quasiparticle and pair densities of states calculated here deviate significantly from the homogeneous (BCS) case—this deviation is a characteristic result for any multilayer. Section V discusses and summarizes the work. Taking proper account of spatial variation not only leads to predictions for multilayer performance for Q and τ_r that are surprising at first sight, but also predicts significant *benefits* from using multilayers as detectors operating below 90 GHz.

II. THEORY

A. Usadel equation and self-consistency

Our analysis of multilayers is based on Usadel's model for the generalized proximity effect in the dirty-limit. Layer boundaries within multilayer structures function as scattering centers and ensure that the behavior of the structure is governed by dirty-limit equations.[22] The one-dimensional Usadel equation states that[21–24]

$$\hbar D_S \frac{\partial}{\partial x}\left(\hat{G}\frac{\partial}{\partial x}\hat{G}\right) = [\hbar\omega_n\sigma_z + \hat{\Delta}(x), \hat{G}]. \qquad (1)$$

The matrices are defined such that

$$\hat{G}(x,\hbar\omega_n) = \begin{pmatrix} G & F \\ F^* & -G \end{pmatrix} \text{ and } \hat{\Delta}(x) = \begin{pmatrix} 0 & \Delta(x) \\ \Delta^*(x) & 0 \end{pmatrix},$$

where $\hbar = h/2\pi$, subscript S denotes the layer of the material, $\omega_n = 2\pi k_B T\left(n+\frac{1}{2}\right)/\hbar$ are the Matsubara frequencies, $n = 0, 1, 2\ldots$, σ_z is the Pauli matrix, $\Delta(x)$ is the superconducting order parameter, and $[a,b] = ab - ba$ is the commutator. $D_S = 2\pi\xi_S^2 T_c k_B/\hbar$ is the diffusion coefficient, where ξ_S is the coherence length. G and F are the normal and anomalous Green's functions and the normalization conditions are $\hat{G}^2 = \hat{1}$, and $G^2 + FF^* = 1$. The analytic continuation of the Green's functions into the continuous domain of quasiparticle energies E is achieved by $\hbar\omega_n \to -iE$ in Eq. (1).

In the θ-parameterization, which automatically satisfies the normalization conditions, we have

$$\hat{G}(x,\hbar\omega_n) = \begin{pmatrix} \cos\theta & \sin\theta \\ \sin\theta & -\cos\theta \end{pmatrix},$$

where $\theta = \theta(x,\hbar\omega_n)$. This yields the θ-parameterized Usadel equation

$$\frac{\hbar D_S}{2}\frac{\partial^2\theta}{\partial x^2} = \hbar\omega_n\sin\theta - \Delta(x)\cos\theta. \qquad (2)$$

Eq. 2 needs to be solved along with the superconducting self-consistency equation

$$\Delta(x)\ln\left(\frac{T_c}{T}\right)-2\pi k_B T\sum_{\omega_n>0}\left(\frac{\Delta(x)}{\hbar\omega_n}-\sin\theta\right)=0, \quad (3)$$

subject to appropriate boundary conditions (BCs) introduced in Ref. [28]. At the open boundaries of the S or S′ layers of bilayer S′ − S or trilayer S − S′ − S structures, the BCs are

$$\frac{\partial\theta_{S,S'}}{\partial x}=0. \quad (4)$$

At the S − S′ interfaces,

$$\frac{1}{\rho_S}\frac{\partial\theta_S}{\partial x}=\frac{1}{\rho_{S'}}\frac{\partial\theta_{S'}}{\partial x}, \quad (5)$$

$$\gamma_{B,S}\xi_S\frac{\partial\theta_S}{\partial x}=\sin(\theta_{S'}-\theta_S). \quad (6)$$

At the S′ − S interfaces,

$$\gamma_{B,S'}\xi_{S'}\frac{\partial\theta_{S'}}{\partial x}=\sin(\theta_S-\theta_{S'}). \quad (7)$$

Here $\gamma_{B,S}=R_B/(\rho_S\xi_S)$ is a measure of boundary resistivity, $\rho_{S,S'}$ are the normal-state resistivities of S, S′ layer, and R_B is the product of the boundary resistance between the S − S′ layers and its area.

Finally, the quasiparticle density of states is given by $N(x,E)=N_0(x)Q(x,E)$, where $Q(x,E)=\mathrm{Re}[\cos\theta(x,E)]$, and $N_0(x)$ is the position-dependent single spin density of electron states. We define the pair-breaking threshold $2\Delta_g$ for the proximity structure as twice the energy for which the DoS becomes appreciably non-zero ($N/N_0>\delta$), where δ is the numerical precision.

B. Nam's formulation for conductivities

Nam's equations[29] are a generalization of the Mattis-Bardeen[30] theory into strong-coupling and impure superconductors. The real and imaginary parts of the complex conductivity $\sigma=\sigma_1-j\sigma_2$ can be expressed as

$$\begin{aligned}\frac{\sigma_1(\nu)}{\sigma_N}=&\frac{1}{h\nu}\int_{\Delta_g-h\nu}^{-\Delta_g}dE\,g_1(E,h\nu+E)\\&[1-2f(E+h\nu,T)]\\&+\frac{2}{h\nu}\int_{\Delta_g}^{\infty}dE\,g_1(E,h\nu+E)\\&[f(E,T)-f(E+h\nu,T)],\end{aligned} \quad (8)$$

$$\begin{aligned}\frac{\sigma_2(\nu)}{\sigma_N}=&\frac{1}{h\nu}\int_{\Delta_g-h\nu,-\Delta_g}^{\Delta_g}dE\,g_2(E,h\nu+E)\\&[1-2f(E+h\nu,T)]\\&+\frac{1}{h\nu}\int_{\Delta_g}^{\infty}dE\\&\{g_2(E,h\nu+E)\,[1-2f(E+h\nu,T)]\\&+g_2(h\nu+E,E)\,[1-2f(E,T)]\},\end{aligned} \quad (9)$$

where the lower limit of the first integral in Eq. (9) refers to the larger of the two energies $\Delta_g-h\nu$ and $-\Delta_g$, and $f(E,T)$ is the Fermi distribution function.The coherence factors $g_{1,2}$ are given by

$$g_1(E,h\nu+E)=Q(E)Q(h\nu+E)+P(E)P(h\nu+E),$$
$$g_2(E,h\nu+E)=-\tilde{Q}(E)Q(h\nu+E)-\tilde{P}(E)P(h\nu+E),$$

where $Q(E)$, $\tilde{Q}(E)$, $P(E)$, $\tilde{P}(E)$, are the generalized quasiparticle and pair densities of states

$$Q(E)+j\tilde{Q}(E)=\mathrm{Re}[\cos\theta(E)]+j\,\mathrm{Im}[\cos\theta(E)]$$
$$P(E)+j\tilde{P}(E)=\mathrm{Re}[-j\sin\theta(E)]+j\,\mathrm{Im}[-j\sin\theta(E)].$$

C. Surface Impedance, Transfer Matrices and Quality Factor

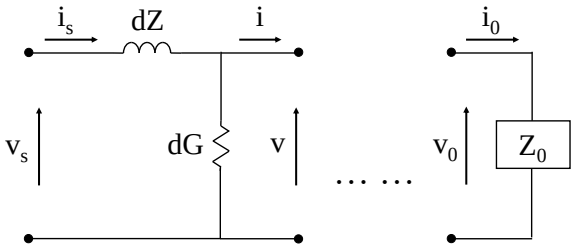


FIG. 1. Transmission line representation of a multilayer as a combination of layers of thickness dx, terminated at vacuum of impedance Z_0.

In order to calculate Zs, we use a transmission line model where the multilayer is sub-divided into a combination of thin layers[31] each represented by an equivalent circuit of series impedance $dZ=j2\pi\nu\mu_0 dx$ and shunt admittance $dG=\sigma(\nu,x)dx$, terminating at vacuum, as shown in Fig. 1. We represent the thin layers by transmission (ABCD) matrices.[32] Cascading the resulting matrices of all layers we have

$$\begin{bmatrix}v_s\\i_s\end{bmatrix}=\prod_{all\ layers}\begin{bmatrix}1&j2\pi\nu\mu_0 dx\\\sigma(\nu,x)dx&1\end{bmatrix}\begin{bmatrix}v_0\\i_0\end{bmatrix}, \quad (10)$$

where $v_0/i_0=Z_0$ is the impedance of free space. The surface impedance is then $Z_s=v_s/i_s$. The layer facing the incoming field corresponds to the left-most matrix in the cascaded multiplication chain. In this way calculation of Z_s for multilayers straightforwardly takes account of the physical ordering of high and low conductivity films with respect to the incident field. The model described is a full calculation of Z_s and reduces to the expressions in Ref. [31] for homogeneous superconducting films in all limits.

We quantify Q for a multilayer resonator used as a KID with the surface impedance quality factor[1] $Q_{\rm s}(\nu) = \mathrm{Im}(Z_{\rm s})/\,\mathrm{Re}(Z_{\rm s})$. $Q_{\rm s}$ is representative of the achievable Q, capturing the underlying physics of the spatially-dependent energy storage and loss in the multilayer, and is related to Q via Eq. (20-21) of Ref. [1]. A complete model to calculate Q would require a full electromagnetic model of the KID geometry (be-it microstrip, coplanar waveguide, lumped-element KID etc.) including electromagnetic coupling and field-fringing effects, but this is beyond the scope of this work. Our calculations of $Z_{\rm s}$ for superconducting multilayers will enable full electromagnetic modeling to be done *for the first time*.

D. Multilayer-averaged Quasiparticle Recombination Times

We use the low-energy expression for quasiparticle recombination time given by Ref. [33] and the material-characteristic electron-phonon coupling time constant τ_0 as described by Kaplan *et al.*.[34] We ignore quasiparticle scattering, which becomes very slow at low temperatures for low energy quasiparticles.[34] The recombination lifetime is given by

$$\frac{\tau_0(x)}{\tau_{\rm r}(x,E)} = \frac{1}{(k_{\rm B}T_{\rm c})^3[1-f(E,T)]}\int_{E+\Delta_{\rm g}(x)}^{\infty} d\Omega\,\Omega^2 \\ [n(\Omega,T)+1]\,f(\Omega-E,T) \\ \left(Q(x,\Omega-E)+\frac{\Delta(x)}{E}P(x,\Omega-E)\right), \quad (11)$$

where Ω is the phonon energy and $n(\Omega,T)$ is the Bose distribution. We note here the change in sign within the final bracket of Eq. (11) compared with Eq. (7d) of Ref. [33]. This ensures that $\tau_{\rm r}$ here reduces to Kaplan's result (Eq. (8), Ref. [34]) with the appropriate expressions for Q and P for homogeneous BCS superconductors.

Assuming thermal equilibrium, we use $Q(x,E)$ and $f(E,T)$ as weights to obtain the energy-averaged recombination time as a function of position

$$\langle\tau_{\rm r}(x)\rangle_E = \frac{\int_{\Delta_{\rm g}(x)}^{\infty}\tau_{\rm r}(x,E)N_0(x)Q(x,E)f(E,T)\,dE}{\int_{\Delta_{\rm g}(x)}^{\infty}N_0(x)Q(x,E)f(E,T)\,dE}. \quad (12)$$

Applying weighted averaging over both energy and position, the multilayer-averaged quasiparticle recombination time is obtained,

$$\langle\tau_{\rm r}\rangle_{E,x} = \frac{\int\int_{\Delta_{\rm g}(x)}^{\infty}\tau_{\rm r}(x,E)N_0(x)Q(x,E)f(E,T)\,dE\,dx}{\int\int_{\Delta_{\rm g}(x)}^{\infty}N_0(x)Q(x,E)f(E,T)\,dE\,dx}. \quad (13)$$

For thin films at low temperatures where $\langle\tau_r\rangle_{E,x} \gg d^2_{\rm Al,Ti}/2D_{\rm Al,Ti}$, Eq. 13 represents the best-estimate of the overall quasiparticle recombination time, including the effect of quasiparticle trapping, provided the number of excess quasiparticles is small such that recombination with thermal quasiparticles dominates. A full solution for strong non-equilibrium conditions, such as high loading or strong pulses, requires solving the self-consistency equation with the kinetic equations describing quasiparticle and phonon coupling,[35] and is beyond the scope of the current work.

III. METHODOLOGY

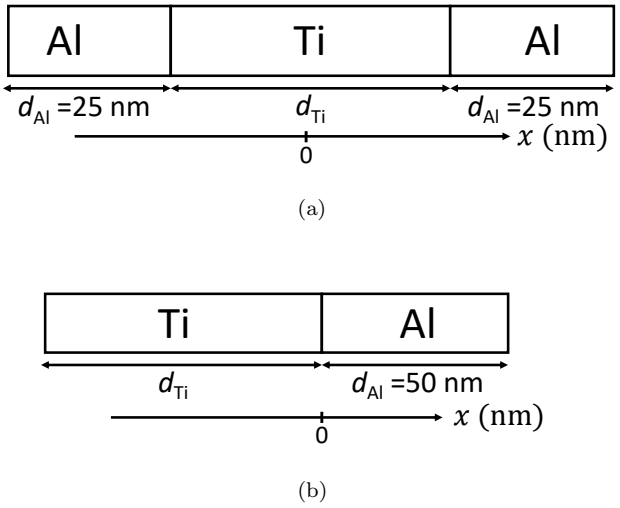


FIG. 2. (a) The geometry of trilayer Al − Ti − Al devices. Al layers have $d_{\rm Al} = 25\,$nm. The central Ti thickness is $d_{\rm Ti}$. Position is denoted by coordinate x which is zero at the centre of the Ti layer. (b) The geometry of bilayer devices. The Al has $d_{\rm Al} = 50\,$nm. $x = 0$ coincides with the Ti − Al interface.

TABLE I. Table of physical parameters of material properties.

	Aluminium	Titanium
$T_{\rm c}$ (K)	1.2[1]	0.4[1]
$\Delta_{\rm g}$ (μeV)	182	61
$\nu_{\rm g}$ (GHz)	88	29
ξ (nm)	170[2]	110[2]
N_0 (10^{23}/eV cm^3)	0.174[1]	0.41[1]
V (10^{-23} eV cm^3)	0.960[1]	0.344[1]
Θ_D (K)	423[1]	426[1]
$\sigma_{\rm N}$ ($/\mu\Omega\,$m)	180[3]	3[4]
τ_0 (ns)	395[5]	7960[5]
RRR	5.5[3]	3.5[6]

[1] Reference [36].
[2] Calculated using dirty limit expression for ξ from Ref. [22].
[3] Measurements by the Cambridge Quantum Sensors Group.
[4] Reference [37].
[5] Reference [38].
[6] Reference [39]

The Usadel equation (2) and the self-consistency equation (3) are solved iteratively, with appropriate BCs, for

Ti − Al bilayers and Al − Ti − Al trilayers with the geometry shown in Fig. 2, at $T = 0.1\,\mathrm{K}$ and $\gamma_{\mathrm{B,Al}} = 0.01$ or $\gamma_{\mathrm{B,Al}} = 100$ to represent both high and low transmission interfaces. Our solver uses MATLAB's multipoint boundary value problem numerical solver. The solver computes the residuals using geometry-specific boundary function handles, to ensure that the solution satisfies Eqs. (4) to (7). The detailed steps of our implementation are as follows:

(i) A uniform trial $\Delta(x) = (\Delta_{\mathrm{Al}} + \Delta_{\mathrm{Ti}})/2$ is used to solve for $\theta(x, \hbar\omega_n)$, using Eq. (2) with maximum $n = 125$. $\theta(x, \hbar\omega_n)$ is then used to solve for $\Delta(x)$ using Eq. (3). The solution then updates $\Delta(x)$.

(ii) An iterative loop of step (i) continues until convergence is achieved in $\Delta(x)$, such that the relative change in $\Delta(x)$ between the final two iterations is less than 0.001%.

(iii) The Usadel equation is then solved *once* using $\Delta(x)$ from (ii) in the domain of continuous quasiparticle energy E to obtain $\theta(x, E)$. This is done by applying $\hbar\omega_n \to -iE$ to Eq. (2).

(iv) Other properties, i.e. $\sigma_{1,2}, Z_{\mathrm{s}}, Q_{\mathrm{s}}$, and τ_{r}, are calculated from $\theta(x, E)$ using equations described in Sec. II.

A list of basic physical parameters used in this paper can be found in Table I. Data for superconducting coherence lengths are calculated using the dirty limit expression, $\xi = \sqrt{\xi_0 l/3}$, from Ref. [22], where ξ_0 is the BCS coherence length, and l is the electron mean free path. Calculation of ξ is supplemented by Al residual resistivity ratio (RRR_{Al}) from the Cambridge Quantum Sensors Group, Ti residual resistivity ratio (RRR_{Ti}) from Ref. [39], and Ti mean free path at 300K ($l_{\mathrm{Ti,300K}}$) from Ref. [40].

A. Scaling the temperature

We scale the temperature of calculation for both Q_{s} and τ_{r}, in order to remove the effect of reducing ν_{g}. Reducing the temperature of the calculation removes the effect of a reduced Δ_{g} to first-order. The principal temperature dependence of both Q_{s} and τ_{r} arises from the Fermi functions in Eqs. 8, 9 and 12 leading to a close-to $\exp(-\Delta_{\mathrm{g}}/k_{\mathrm{B}}T)$ dependence at a *fixed* T in both cases. Scaling T removes this effect, giving comparable operating regimes but it also means that in practice lower experimental temperatures are required. For Al, we choose $T = 170$ mK i.e. close to the onset of the experimentally-observed low-temperature limit of τ_{r} seen in all low-T_{c} superconductors .[1,4,41] The limiting temperature scales as T/T_{c} for many low temperature superconductors, although we are unaware of similar measurements in multilayers. For all multilayers, the temperature is scaled such that $T = 170\ \mathrm{mK} \times (\Delta_{\mathrm{g}}/\Delta_{\mathrm{Al}})$. Even-so, for the thickest trilayer with threshold as low as $\nu_{\mathrm{g}} = 50$ GHz an operating temperature $T = 95$ mK would be sufficient, well-above the experimentally accessible range using an ADR.

IV. RESULTS

A. Density of states gap and pair-breaking threshold

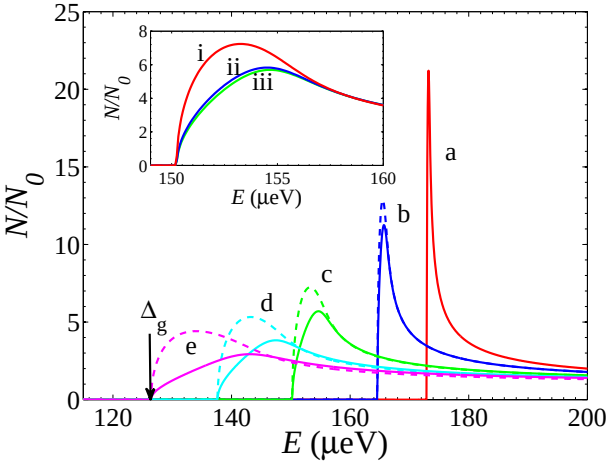


FIG. 3. DoS for 5 Al − Ti − Al *trilayers* at the open boundary of the Al (solid lines) and at the centre of the Ti (dashed lines). (a) red line, $d_{\mathrm{Ti}} = 25\,\mathrm{nm}$, (b) blue line, $d_{\mathrm{Ti}} = 50\,\mathrm{nm}$, (c) green line, $d_{\mathrm{Ti}} = 100\,\mathrm{nm}$, (d) cyan line, $d_{\mathrm{Ti}} = 150\,\mathrm{nm}$, and (e) purple line, $d_{\mathrm{Ti}} = 200\,\mathrm{nm}$. The total Al thickness is 50 nm, $T = 0.1$ K and $\gamma_{\mathrm{B,Al}} = 0.01$. The inset shows the DoS at different positions of a 25nm − 100nm − 25nm multilayer. (i) red line, centre of Ti layer, (ii) blue line, Ti-side of internal Ti-Al interface and, (iii) green line, external Al boundary . $T = 0.1$ K and $\gamma_{\mathrm{B,Al}} = 0.01$.

Figure 3 shows the normalized densities of states (DoS) for 5 Al − Ti − Al trilayers with Ti thicknesses, (a) to (e), 25, 50, 100, 150 and 200 nm respectively, at the open Al boundaries (solid lines) and at the centre of the Ti layer (dashed lines). The total Al thickness is 50 nm. The DoS is BCS-like for the thinnest Ti layer (trace (a)) due to both d_{Al} and d_{Ti} being much smaller than their respective coherence lengths. The DoS broadens for thicker Ti films. For very thick Ti layers (not shown) the DoS at the Ti layer tends to the BCS DoS for Ti, whereas the DoS at edge of the Al broadens further and does not tend to any BCS limit. The broadening behaviour highlights the need for a rigorous model beyond BCS-like DoS approximations. In this numerical study, we use $\delta = 0.01$ to determine the pair-breaking threshold $2\Delta_{\mathrm{g}}$. For clarity we have only indicated this for trace (e). The inset shows the DoS at different positions within the 25nm − 100nm − 25nm multilayer. Trace (i) shows the

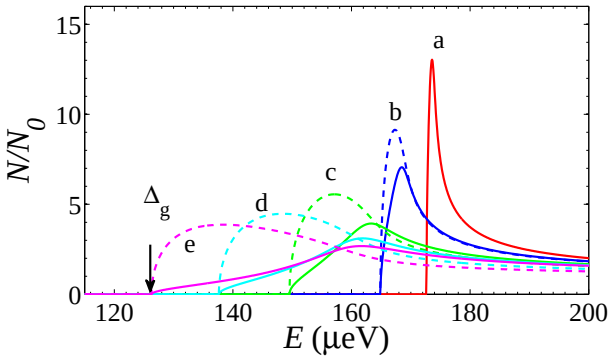


FIG. 4. DoS for 5 Ti − Al *bilayers* at the open boundary of the Al (solid lines) and at the open boundary of the Ti (dashed lines). (a) red line, $d_{\rm Ti} = 25$ nm, (b) blue line, $d_{\rm Ti} = 45$ nm, (c) green line, $d_{\rm Ti} = 80$ nm, (d) cyan line, $d_{\rm Ti} = 105$ nm, and (e) purple line, $d_{\rm Ti} = 130$ nm. The total Al thickness is 50 nm, $T = 0.1$ K and $\gamma_{\rm B,Al} = 0.01$.

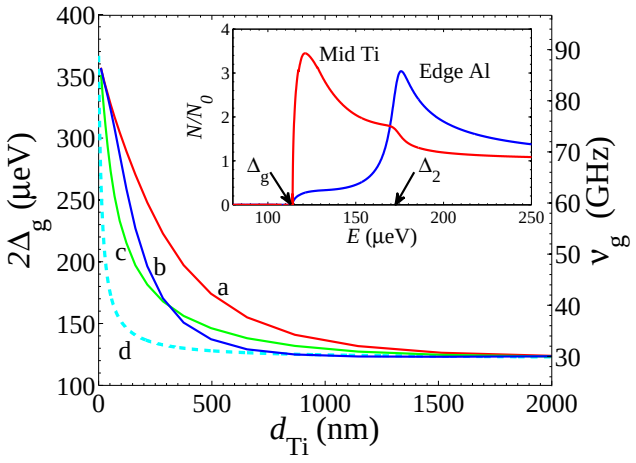


FIG. 5. Pair-breaking threshold $2\Delta_{\rm g}$ as a function of central Ti thickness with fixed total Al thickness 50 nm. (a) red line, trilayer with $\gamma_{\rm B,Al} = 0.01$, (b) blue line, bilayer with $\gamma_{\rm B,Al} = 0.01$, (c) green line, trilayer with $\gamma_{\rm B,Al} = 100$, and (d) cyan line, weighted-average model. $T = 0.1$ K. The inset shows the DoS for trilayer of 25nm − 100nm − 25nm geometry at middle of Ti layer (red) and edge of Al layer (blue), $\gamma_{\rm B,Al} = 100$.

DoS at the centre of Ti layer, (ii) the DoS at the Ti-side of the internal Ti-Al interface, (iii) the DoS at the external Al boundary. The DoS does not vary greatly with position in the Al layer. The high Al normal-state conductivity, compared to Ti, restricts the extent of variation of DoS in the Al layer. The DoS at different positions along the same device share a common energy gap because all films are relatively thin ($d \sim \xi$).

Figure 4 shows the DoS for 5 Ti − Al bilayers of Al thicknesses, (a) to (e), 25, 45, 80, 105 and 130 nm respectively at the open Al boundaries (solid lines) and at the open Ti boundaries (dashed lines). Ti thicknesses for the bilayers were chosen to give the same pair-breaking thresholds as the trilayers. A key difference between bi- and trilayers with equal $\Delta_{\rm g}$ is the reduction in the DoS in the Al layer near $\Delta_{\rm g}$ for bilayers. At large values of $d_{\rm Ti}$, the reduction is more pronounced as individual Al layer thicknesses (instead of total Al layer thickness) becomes more important to the DoS. This reduction in the DoS has immediate impact on the thermal quasiparticle density $N_{\rm th}(x) = 4\int N_0 Q(x,E) f(E,T)\, dE$ in the Al and likewise changes σ and $\tau_{\rm r}$.

Figure 5 shows the pair-breaking threshold $2\Delta_{\rm g}$ (the right-hand scale shows $\nu_{\rm g}$) for: (a) red line, Al − Ti − Al trilayer with $\gamma_{\rm B,Al} = 0.01$, (b) blue line, Ti − Al bilayer with $\gamma_{\rm B,Al} = 0.01$, (c) green line, Al − Ti − Al trilayer with $\gamma_{\rm B,Al} = 100$, and (d) cyan dashed line, weighted-average model. In all cases $T = 0.1$ K and the total Al thickness is 50 nm. Comparing (a) with (b) we see that the thresholds for bi- and trilayers are not the same and the bilayer gap is *lower* with the same Ti thickness and interface transparency. This is a direct result of the BCs Eqs. (4) to (7) and self-consistency Eq. (3). Al as the outer layers of a trilayer acts to increases $\Delta(x)$ in the Ti from both sides, whereas the external BCs for Ti in a bilayer cannot. Comparing (a) with (c) where $\gamma_{\rm B,Al} = 0.01,\ 100$ respectively representing a clean, high-transmission or a dirty, low-transmission interface, we see that the threshold is reduced as the interface becomes less transmissive. In other simulations we find that $\Delta_{\rm g}$ is a weak function of $\gamma_{\rm B,Al}$ provided $\gamma_{\rm B,Al} \lesssim 1$. Comparing all of (a)-(c) with (d) the weighted-average model, we see that the latter significantly *over-estimates* the efficiency of the proximity effect in reducing $\Delta_{\rm g}$. In this analysis, the fixed total Al thickness at 50 nm results in deviation from the weighted-average model, even when coupled with very thin Ti layer. The weighted-average model gives the same prediction for *both* bi- and trilayers because the total Al thickness is fixed: the detail imposed by the geometry is lost. It can be seen from all of (a) to (c) that the proximity effect is a long range *diffusive* process that extends over much longer distances than the component coherence lengths.

The inset shows the DoS for a trilayer of 25 nm − 100 nm − 25 nm geometry at the centre of the Ti layer (red line) and the outer boundary of the Al layer (blue line), calculated for $\gamma_{\rm B,Al} = 100$. In this case, where the film coupling is weak, the DoS across the multilayer shows more structure with two relatively broad peaks, the first somewhat greater than $\Delta_{\rm g}$ and the second Δ_2 close to $\Delta_{\rm Al}$. The DoS at the centre of the Ti increases significantly from zero at Δ_g, and shows a small increase at Δ_2. The DoS at the edge of the Al increases slowly from zero at Δ_g and shows a large increase at Δ_2. For very low transmission boundaries $\gamma_{\rm B,Al} \to \infty$, the DoS at the middle of the Ti increases exclusively at $\Delta_g = \Delta_{\rm g,Ti}$ whilst the DoS at the edge of the Al increases exclusively at $\Delta_2 = \Delta_{\rm g,Al}$, the proximity coupling disappears in this case and we find a BCS-like DoS for the individual layers.

The overall effect on KID performance as a result of

these spatially varying DoS with $d_{\rm Ti}$ is not obvious at first sight. In the next sections we explore the impacts on $Z_{\rm s}$, $Q_{\rm s}$ and $\tau_{\rm r}$ for bi- and trilayers.

B. Conductivity, Impedance and Quality Factor

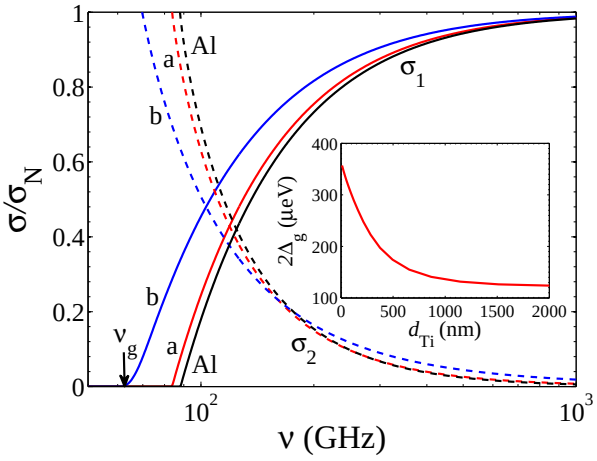


FIG. 6. Normalized real (solid line) and imaginary (dashed line) conductivities for two trilayers, (a) red line, $d_{\rm Ti} = 25$ nm, (b) blue line, $d_{\rm Ti} = 200$ nm. The black lines are calculated for Al. $T = 0.1$ K, and $\gamma_{\rm B,Al} = 0.01$. The total Al thickness is 50 nm. The inset shows the variation of $2\Delta_{\rm g}$ as a function of $d_{\rm Ti}$.

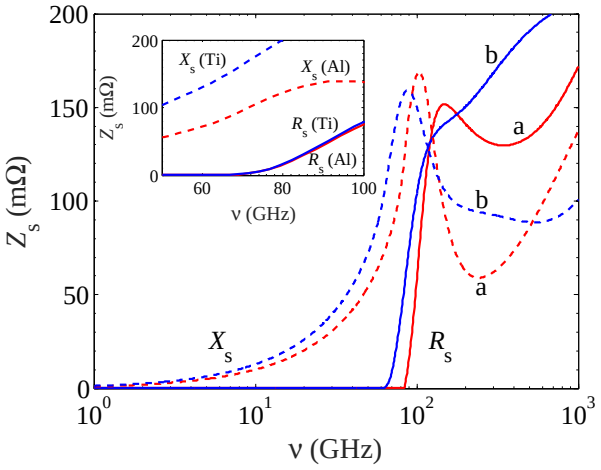


FIG. 7. Frequency dependence of $R_{\rm s}$ (solid line) and $X_{\rm s}$ (dashed line) for two trilayers: (a) red line, $d_{\rm Ti} = 25$ nm, (b) blue line, $d_{\rm Ti} = 200$ nm. $T = 0.1$ K and $\gamma_{\rm B,Al} = 0.01$ and $d_{\rm Al} = 25$ nm. The inset shows the variation of $R_{\rm s}$ (solid lines) and $X_{\rm s}$ (dashed lines) for a bilayer with $d_{\rm Ti} = 130$ nm, at frequencies close to $\nu_{\rm g} = 61$ GHz. The blue lines indicate incidence on the Ti surface, the red lines indicate incidence on the Al surface.

Figure 6 shows normalized conductivities $\sigma/\sigma_{\rm N}$ as a function of ν for two trilayers with (a) $d_{\rm Ti} = 25$, and (b) 200 nm. The total Al thickness is 50 nm. Full lines show σ_1 and dashed lines σ_2. The black lines show calculations for Al for comparison. In all cases $T = 0.1$ K and $\gamma_{\rm B,Al} = 0.01$ and $d_{\rm Al} = 50$ nm. Also indicated is $\nu_{\rm g}$ for the 25 nm − 200 nm − 25 nm trilayer. The ratio $\sigma_1/\sigma_{\rm N}$ is identical to the superconducting to normal-state photon absorption ratio.[14] $\sigma_1/\sigma_{\rm N}$ has a threshold at $\nu_{\rm g} = 2\Delta_{\rm g}/h$ and shows a slow increase above threshold. As a result, although Al KIDs have $\nu_{\rm g} = 88$ GHz, they only operate efficiently above 100 GHz or even 120 GHz.[8] We find that changes in the normalized $\sigma/\sigma_{\rm N}$ are small as a function of position within a particular bi- or trilayer, and thus we have not shown these results. This is a result of the highly-transmissive interfaces. However, the absolute values of σ are very different in the Al and Ti layers due to the very different values of $\sigma_{\rm N}$.

Figure 7 shows the frequency dependence of the real and imaginary parts of $Z_{\rm s} = R_{\rm s} + jX_{\rm s}$ for 2 trilayers with (a) $d_{\rm Ti} = 25$, and (b) 200 nm. Here ν is chosen to emphasize *signal* frequencies. The structure evident in $R_{\rm s}$ and $X_{\rm s}$ above $\nu_{\rm g}$ arises because *both* the DoS and $\sigma_{\rm N}$ are dependent on position. This structure would be absent if a simple BCS-like DoS were assumed to carry out the calculation of $R_{\rm s}$ and $X_{\rm s}$. The surface resistance $R_{\rm s}$ decreases sharply with decreasing frequencies near $\nu_{\rm g}$, and tends-to zero below $\nu_{\rm g}$ as $\exp(-\nu_{\rm g}/k_{\rm B}T)$. We find that contributions from the Al layers to $Z_{\rm s}$ are more important by virtue of its higher $\sigma_{\rm N}$ compared to Ti. Interestingly, at low frequencies, the thickest trilayer (blue line) has the lowest dissipative component $R_{\rm s}$ (barely visible) and highest reactive component $X_{\rm s}$. The inset of Fig. 7 shows the variation of $R_{\rm s}$ and $X_{\rm s}$ for a bilayer with $d_{\rm Ti} = 130$ nm, at frequencies close to $\nu_{\rm g} = 61$ GHz. $R_{\rm s}$ is almost independent of orientation, while $X_{\rm s}$ shows significant differences when a bilayer is illuminated from different sides. This highlights the need to properly account for geometry when modeling multilayer resonators.

In order to show the effect on the detection sensitivity of a KID fabricated from these bi- and trilayers, in Fig. 8 we plot $Q_{\rm s}$, at scaled temperatures in the range of 100 mK for the lowest gap multilayers up to 170 mK for Al. $Q_{\rm s}$ increases by a factor $\simeq 2$ as $d_{\rm Ti}$ increases from 25 to 200 nm. Changing the thickness of an Al KID by the

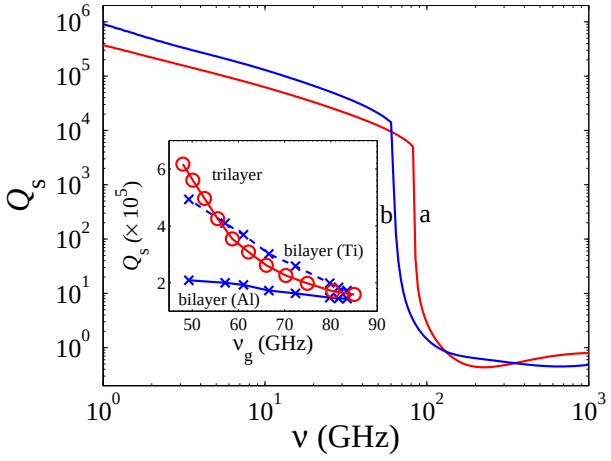


FIG. 8. Frequency dependence of Q_s for trilayers with varying d_{Ti}. (a) red line, $d_{Ti} = 25$ nm, (b) blue line, $d_{Ti} = 200$ nm. $T = 0.1$ K, $\gamma_{B,Al} = 0.01$, with total Al thickness of 50 nm. The inset shows the variation of Q_s with $\nu = 3$ GHz as a function of ν_g: (red solid line) trilayers, (blue solid line) bilayers with incidence on the Al surface, (blue dashed line) bilayers with incidence on the Ti surface. The temperature of the calculation is scaled such that $T = 170$ mK $\times (\Delta_g/\Delta_{Al})$ for all multilayers.

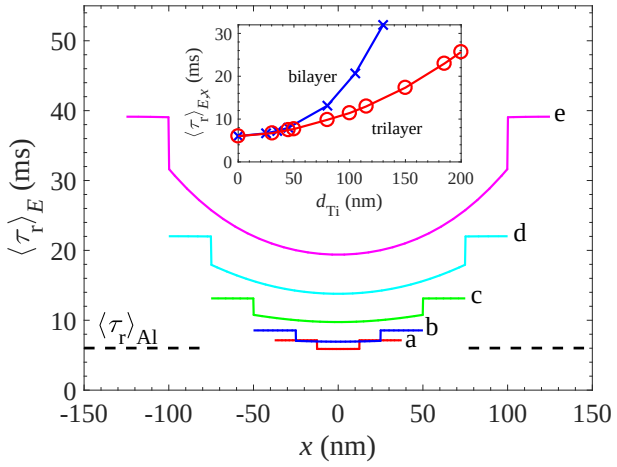


FIG. 9. Energy-averaged recombination times $\langle\tau_r\rangle_E$ for five proximity trilayers of Al − Ti − Al geometry, compared to that of thin-film Al (dashed line), as a function of position x. (a) red line, $d_{Ti} = 25$ nm, (b) blue line, $d_{Ti} = 50$ nm, (c) green line, $d_{Ti} = 100$ nm, (d) cyan line, $d_{Ti} = 150$ nm, and (e) purple line, $d_{Ti} = 200$ nm. $\gamma_{B,Al} = 0.01$. The temperature of the calculation is scaled such that $T = 170 \times (\Delta_g/\Delta_{Al})$ mK for each trilayer. The inset shows multilayer-averaged recombination times $\langle\tau_r\rangle_{E,x}$ as a function of Ti thickness for (i) red line, trilayer with total Al layer thickness 50 nm, (ii) blue line, bilayer with Al layer thickness 50 nm.

same amount would change Q_S by a factor $\simeq 3$. From the point-of-view of KID operation this begins to suggest that there is little penalty in device sensitivity even having engineered the reduced threshold.

The inset of Fig. 8 shows Q_s at $\nu = 3$ GHz representing a typical KID readout frequency, as a function of threshold ν_g. The solid blue line shows Q_s for bilayers with the field incident on the Al surface, the dashed blue line shows Q_s for bilayers with field incident on the Ti surface. In both cases as ν_g is reduced Q_s increases due to the increase in total thickness but note that the geometry— in this case the ordering with respect to the incident field— also affects Q_s. The effect of increasing d_{Ti} is more significant when the field interacts from the Ti side. The solid red line shows Q_s for Al-Ti-Al trilayers. At high thresholds $\nu_g \sim 70$ GHz, corresponding to thin Ti layers, Q_s for the trilayer lies between the bilayer Q-values. The increase of the trilayer Q_s compared to bilayers at low ν_g can be understood from Fig. 5: a thicker Ti layer is required in trilayers to achieve the same ν_g. Two points are important. Q_s for multilayer resonators with low ν_g remain highly-suitable for KIDs. The ordering of a *bilayer* with respect to the field is also important to maximizing Q_s. This emphasizes the need for full electromagnetic modeling of the field distributions.

C. Quasiparticle Lifetimes in Multilayers

Here we show results of calculations of energy- and multilayer-averaged recombination times $\langle\tau_r(x)\rangle_E$ and $\langle\tau_r\rangle_{E,x}$ respectively. For all multilayers, the temperature is scaled such that $T = 170$ mK $\times (\Delta_g/\Delta_{Al})$.

Figure 9 shows $\langle\tau_r(x)\rangle_E$ as a function of position for *trilayers* with five Ti thicknesses (a) to (e) 25, 50, 100, 150 and 200 nm respectively and, for comparison, calculation for Al. For the thinnest trilayer, Fig. 9 (a) $\langle\tau_r\rangle_E$ is close-to the calculated value for Al. For thicker trilayers $\langle\tau_r\rangle_E$ *increases* in both the Al and Ti layers. This arises from the reducing quasiparticle density of states in the Al at low energies as d_{Ti} increases (see Fig. 3), and the combined effect of the reduced lower limit of the integral in Eq. (11) and the Ω^2 dependence of the phonon density of states factor within that integral. The situation is similar for bilayers.

Figure 10 shows $\langle\tau_r(x)\rangle_E$ as a function of position for

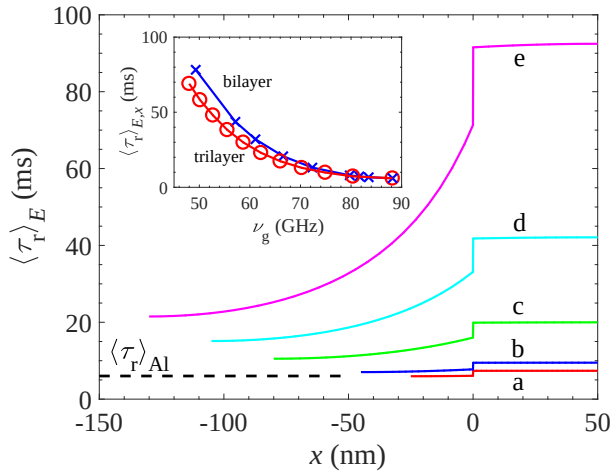


FIG. 10. Energy-averaged recombination times $\langle\tau_r\rangle_E$ for five proximity bilayers of Ti − Al geometry, compared to that of thin-film Al (dashed line), as a function of position x. (a) red line, $d_{Ti} = 25$ nm, (b) blue line, $d_{Ti} = 45$ nm, (c) green line, $d_{Ti} = 80$ nm, (d) cyan line, $d_{Ti} = 105$ nm, and (e) purple line, $d_{Ti} = 130$ nm. $\gamma_{B,Al} = 0.01$. The temperature of the calculation is scaled such that $T = 170$ mK $\times (\Delta_g/\Delta_{Al})$ for each bilayer. The inset shows multilayer-averaged recombination times $\langle\tau_r\rangle_{E,x}$ as a function of ν_g for (i) red line, trilayer with total Al layer thickness 50 nm, (ii) blue line, bilayer with Al layer thickness 50 nm.

bilayers for five Ti thicknesses (a) to (e) 25, 45, 80, 105 and 130 nm respectively and $d_{Al} = 50$ nm. The Ti thicknesses are chosen so that ν_g for (a) to (e) in Fig. 10 are the same as (a) to (e) in Fig. 9. Although similar, in detail we see that the bilayer recombination times are now *longer* in both the Ti and Al compared to trilayers with the *same* ν_g. This arises from the reduced DoS in the Al in bilayers compared to trilayers with the same ν_g, noted earlier in Sec. IV A. This emphasizes the importance of a full calculation of the spatially-dependent DoS.

The inset of Fig. 9 shows $\langle\tau_r\rangle_{E,x}$ as a function of d_{Ti} for bilayers and trilayers. As expected from the main plots, $\langle\tau_r\rangle_{E,x}$ increases with d_{Ti} and for bilayers the increase is more rapid. The behaviour here can be understood from Fig. 5, Δ_g changes more quickly with d_{Ti} for bilayers than trilayers. The detailed differences arise from the different d_{Ti} required to achieve a given ν_g in the two instances, the differing spatial variations in the DoS in Al and Ti, (in particular the reduced Al DoS in a bilayer having the same ν_g —compare Figs. 3 and 4), and also the effect of the weighting with N_0 and d_{Ti} used in the calculation of $\langle\tau_r\rangle_{E,x}$ in Eq. (13).

The inset of Fig. 10 shows $\langle\tau_r\rangle_{E,x}$ as a function of the experimental requirement ν_g for both bilayers and trilayers. We find that bilayers and trilayers with the same ν_g have very similar multilayer-averaged recombination times, the bilayer being of order 20% longer, so that both behave comparably. The choice between them can be made on the basis of other considerations - ease of deposition or material processing or film thickness requirements for example. We have not included the effect of phonon-trapping in these calculations.[42] For thicker multilayers we would expect phonon-trapping to provide an additional enhancement of the effective quasiparticle lifetime.

V. DISCUSSION AND CONCLUSIONS

We have described a full analysis of multilayer resonators suitable for KIDs based on the diffusive Usadel equations with appropriate boundary conditions that takes proper account of the spatial variation of the superconducting properties as a function position in the film. We calculate the spatial variation of the superconducting order parameter $\Delta(x)$, the quasiparticle and pair densities of states, the superconducting energy gap Δ_g, the complex conductivity σ, and energy- and multilayer-averaged τ_r for Al-Ti multilayers. We account for the spatial variation of T_c, N_0, normal-state conductivity σ_N, and characteristic quasiparticle lifetime τ_0. We have also described how to calculate the surface impedance Z_s including varying film properties and the ordering of the multilayer with respect to the incident fields. Our predictions of Δ_g differ significantly from earlier predictions that were based on the weighted-average model, and indicate differences between bilayers and trilayers with the same total film thicknesses.

The calculated quasiparticle and pair densities of states for the Al-Ti multilayers considered here deviate significantly from the homogeneous (BCS) case. We predict high quality factors Q_s and long multilayer-averaged quasiparticle recombination times $\langle\tau_r\rangle_{E,x}$ compared to thin-film Al. Following Ref. [2], we define a figure-of-merit for multilayers such that $\mathcal{F}(\nu) \propto Q_s\langle\tau_r\rangle_{E,x}\Theta(\nu - \nu_g)$, where Θ is the Heaviside step function, giving appropriate weight to the required detection threshold. Even without evaluation, considering values of Q_s and $\langle\tau_r\rangle_{E,x}$ shown in Figs. 8 and 10, values of $\mathcal{F}(\nu)$ for Al-Ti multilayers would be comparable to or better than those of Al films whilst achieving the required ν_g. The multilayer structures described in this study are excellent candidates for high-sensitivity, multiplexible KIDs with tar-

geted low-frequency detection thresholds.

Our work demands a programme of theoretical and experimental investigation of proximity-effect resonators for KID applications. For the first time, full electromagnetic modeling of multilayer resonators is possible. We find that full consideration of the field distribution is essential, particularly if bilayers are to be used. We find that in terms of detector sensitivity, there should be little difference in the performance of bi- and trilayers provided the geometry is properly considered. We have also identified relatively simple experimental measurements that would confirm our predictions of multilayer behaviour. Demonstrating high Q and long $\tau_{\rm r}$ in Al-Ti multilayers is critical for KIDs based on multilayers to become the preferred solution for sub-100 GHz detection. Further work is required to optimise device geometry and material combinations for particular applications. Overall, we have described a coherent approach to calculating the properties of superconducting multilayers for use as KIDs for experimentally important applications at frequencies in the range $50 - 100$ GHz.

* sz311@cam.ac.uk

[1] J. Zmuidzinas, Annu. Rev. Condens. Matter Phys. **3**, 169 (2012).
[2] H. G. Leduc *et al.*, Appl. Phys. Lett. **97**, 102509 (2010).
[3] S. Doyle, P. Mauskopf, J. Naylon, A. Porch, and C. Dunscombe, J. Low Temp. Phys. **151**, 530 (2008).
[4] R. Barends *et al.*, J. Low Temp. Phys. **151**, 518 (2008).
[5] R. M. J. Janssen *et al.*, Appl. Phys. Lett. **103** (2013).
[6] P. J. de Visser, J. J. A. Baselmans, J. Bueno, N. Llombart, and T. M. Klapwijk, Nat. Commun. **5** (2014).
[7] Planck HiFi Core Team, Astron. Astrophys. **536**, A4 (2011).
[8] A. Catalano *et al.*, Astron. Astrophys. **580**, A15 (2015).
[9] C. Cicone *et al.*, Astron. Astrophys. **543**, A99 (2012).
[10] C. N. Thomas *et al.*, (2014), astro-ph.IM/1401.4395v1.
[11] J. Mahfouf *et al.*, Q. J. R. Meteorol. Soc. **141**, 3268 (2015).
[12] F. Aires *et al.*, J. Geophys. Res. Atmos. **120**, 11334 (2015).
[13] E. C. Turner *et al.*, Atmos. Meas. Tech. **9**, 5461 (2016).
[14] M. Tinkham, *Introduction to Superconductivity*, 2nd ed. (McGraw-Hill, New York, 1994).
[15] G. Jones *et al.*, astro-ph.IM , 1701.08461v2 (2017).
[16] G. Coiffard *et al.*, J. Low Temp. Phys. **184**, 654 (2016).
[17] M. R. Vissers *et al.*, Thin Solid Films **548**, 485 (2013).
[18] M. R. Vissers *et al.*, Appl. Phys. Lett. **102** (2013).
[19] A. Giachero *et al.*, J. Low Temp. Phys. **176**, 155 (2014).
[20] L. N. Cooper, Phys. Rev. Lett. **6**, 68954 (1961).
[21] K. D. Usadel, Phys. Rev. Lett. **25**, 507 (1970).
[22] G. Brammertz *et al.*, Physica C Supercond. **350**, 227 (2001).
[23] A. A. Golubov, M. Y. Kupriyanov, and E. Il'ichev, Rev. Mod. Phys. **76**, 411 (2004).
[24] A. S. Vasenko, A. A. Golubov, M. Y. Kupriyanov, and M. Weides, Phys. Rev. B **77**, 134507 (2008).
[25] G. Wang *et al.*, IEEE Trans. Appl. Supercon. **27** (2017).
[26] G. Vardulakis, *Superconducting Kinetic Inductance Detectors: Theory, Simulations, and Experiments*, PhD thesis, University of Cambridge, 2007.
[27] A. Monfardini *et al.*, Astrophys. J. Suppl. S. **194** (2011).
[28] M. Y. Kuprianov and V. F. Lukichev, Sov. Phys. JETP **67**, 1163 (1988).
[29] S. B. Nam, Phys. Rev. **156**, 487 (1967).
[30] D. Mattis and J. Bardeen, Phys. Rev. **111**, 412 (1958).
[31] A. R. Kerr, National Radio Astronomy Observatory Report No. 245, 1996 (unpublished).
[32] Kai Chang, *Microwave solid-state circuits and applications* (Wiley, New York, 1994).
[33] A. A. Golubov *et al.*, Phys. Rev. B **49**, 12953 (1994).
[34] S. B. Kaplan *et al.*, Phys. Rev. B **14**, 4854 (1976).
[35] J.-J. Chang and D. J. Scalapino, J. Low Temp. Phys. **31**, 1 (1978).
[36] G. Gladstone, M. A. Jensen, and J. R. Schrieffer, Superconductivity in the transition metals: theory and measurement, in *Superconductivity*, edited by R. D. Parks, pp. 665–816, Marcel Dekker, New York, 1969.
[37] G. Fujii *et al.*, J. Low Temp. Phys. **167**, 815 (2012).
[38] L. Parlato *et al.*, Supercond. Sci. Technol. **18**, 1244 (2005).
[39] D. Fukuda *et al.*, IEEE Trans. Appl. Supercon. **17**, 259 (2007).
[40] C. Reale, Rev. Bras. Fis. **3**, 431 (1973).
[41] P. J. de Visser *et al.*, Phys. Rev. Lett. **112** (2014).
[42] A. Rothwarf and B. N. Taylor, Phys. Rev. Lett. **19**, 27 (1967).